Bridging Particle and Wave Sensitivity in a Configurable Detector of Positive Operator-Valued Measures

Graciana Puentes,* Jeff S. Lundeen, Matthijs P. A. Branderhorst, Hendrik B. Coldenstrodt-Ronge, Brian J. Smith, and Ian A. Walmsley

Clarendon Laboratory, University of Oxford, Parks Road, Oxford OX1 3PU, United Kingdom

(Received 6 October 2008; published 27 February 2009)

We report an optical detector with tunable positive operator-valued measures. The device is based on a combination of weak-field homodyne techniques and photon-number-resolving detection. The resulting positive operator-valued measures can be continuously tuned from Fock-state projectors to a variety of phase-dependent quantum-state measurements by adjusting different system parameters such as local oscillator coupling, amplitude, and phase, allowing thus not only detection but also preparation of exotic quantum states. Experimental tomographic reconstructions of classical benchmark states are presented as a demonstration of the detector capabilities.

DOI: 10.1103/PhysRevLett.102.080404 PACS numbers: 03.65.Wj, 42.50.Ar

Detecting optical fields plays a key role throughout physics. From the definition of the SI unit of luminosity [1] to the characterization of quantum processes such as quantum logic gates [2], precise measurement of the electromagnetic field is central to both fundamental and applied physics. The usual method of measuring fields in optics is either by counting photons or by measuring the amplitude and phase of the electric field. It is usually not possible to move continuously between these two measurement regimes with a single detector. For example, standard homodyne detectors cannot directly probe the particle nature of light since it is masked by the local oscillator and electronic noise [3]. Conversely photon-number-resolving (PNR) detectors possess no phase reference and thus have no sensitivity to the wave nature of light [4].

The action of a given detector can be specified by a positive operator-valued measurement (POVM) set $\{\hat{\Pi}_{\beta\gamma}\}$, where $\{\beta\}$ labels the outcomes and $\{\gamma\}$ labels the settings, such that for each γ the set is complete, $\sum_\beta \hat{\Pi}_{\beta\gamma} = I$ [5]. The probability of obtaining outcome β for setting γ and input state $\hat{\rho}$ is $p_{\beta\gamma} = \mathrm{Tr}[\hat{\Pi}_{\beta\gamma}\hat{\rho}]$. In conventional detectors $\{\hat{\Pi}_{\beta\gamma}\}$ is fixed by the intrinsic nature of the device. Typically, such POVMs can encompass either Fock-state projectors (for PNR detectors) or field-quadrature projectors (for homodyne devices). In this Letter, we report a configurable detector with a flexible POVM, able to transition smoothly from quadrature to photon-number detection. The detector is constructed from a variable reflectivity (R) beam splitter (BS), two PNR detectors, and an auxiliary weak coherent state acting as the local oscillator (LO). We denote such a device as a photon-number-resolving homodyne detector (PNRHD). The BS input modes, labeled $\hat{a}^{\mathrm{in}}$ and $\hat{b}^{\mathrm{in}}$, correspond to the LO and the signal ($\hat{\rho}$), respectively [see Fig. 1(a)]. The output modes, labeled by $\hat{a}^{\mathrm{out}}$ and $\hat{b}^{\mathrm{out}}$, are detected by PNR detectors D_a and D_b giving joint outcomes $\{\beta = (k_a, k_b)\}$, where $k_{a(b)}$ labels the number of clicks registered at $D_{a(b)}$. The adjustable local oscillator has settings $\{\gamma = (|\alpha|, \theta)\}$, where $\alpha = |\alpha|e^{i\theta}$ represents the LO complex amplitude. By tuning the LO coupling, amplitude, and phase the detector POVM set can be configured to project onto a variety of fundamental quantum states of the radiation field—Fock, displaced-Fock, quadrature-squeezed, and macroscopic quantum superposition states, for example. Figures 1(b) and 1(c) depict the Wigner representation [6] of such POVM elements ($\hat{\Pi}_{\beta\gamma}$). Since the action of a measurement is not only to reveal some property of the state of a system, but also to project the system in a state commensurate with that information, all measurement devices may in principle be used as preparation devices. Thus, the remarkable POVM elements of the PNRHD can be used not only to optimally

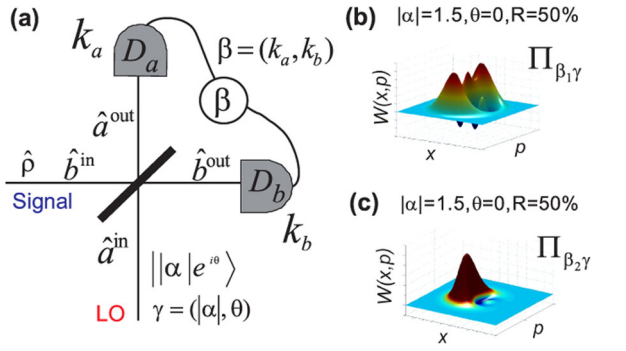

FIG. 1 (color online). (a) Proposed scheme for the POVM configurable detector. D_a and D_b are PNR detectors, α is a weak coherent state. (b),(c) POVM elements $\hat{\Pi}_{\beta\gamma}$ corresponding to click events (b) $\beta_1 = (1, 3)$ and (c) $\beta_2 = (1, 1)$ for LO settings $\gamma = (|\alpha| = 1.5, \theta = 0)$, $R = 50\%$ and 90% efficient PNR detectors. $\hat{\Pi}_{\beta\gamma}$ projects onto a single-mode (b) mesoscopic quantum superposition state and (c) squeezed state, with high probabilities.

detect the appropriate states [7] but also to prepare them from quadrature-entangled beams [8].

As an experimental demonstration of the PNRHD capabilities, we have tomographically reconstructed a group of classical benchmark states. To our knowledge, this constitutes the first full tomographic reconstructions involving PNR detectors. Indeed, state tomography based on photon-counting detection has been the subject of much theoretical work [9], and the few experimental implementations reported to date involve only binary (on-off) detectors [10]. This is due, in part, to the relative infancy of PNR detector technology, which is an active area of research with several different approaches to photon counting [11]. In the experiments presented here time-multiplexed PNR detectors are used, but the techniques can be readily extended to other PNR detectors. The ability to change the measurement basis of the detector enables applications other than state reconstruction for this detection scheme, such as in nonlocal state preparation, precision quantum metrology [12], or the implementation of a continuous-variable entanglement witness [13].

The POVM elements are derived from an analytical model by first considering ideal PNR detectors, able to resolve n photons [see Fig. 1(a)]. In this case the probability of obtaining measurement outcome $\beta = (n_a, n_b)$ for LO setting γ is related to $\hat{\rho}$ by [14]

$$p_{\beta\gamma} = \mathrm{Tr}_{ab}[\hat{U}\hat{\sigma}_{ab}\hat{U}^\dagger |n_a\rangle\langle n_a|_a \otimes |n_b\rangle\langle n_b|_b], \qquad (1)$$

with $\hat{U} = e^{i\xi(\hat{b}^\dagger\hat{a} + \hat{a}^\dagger\hat{b})}$ the unitary operator representing the BS, $R = \cos^2(\xi)$ the LO coupling, $\hat{\sigma}_{ab} = |\alpha\rangle\langle\alpha|_a \otimes \hat{\rho}_b$ the two-mode input state, and $|n_{a(b)}\rangle$ the photon-number states to be detected at $D_{a(b)}$. Using cyclic properties of the trace, Eq. (1) can be written as $p_{\beta\gamma} = \mathrm{Tr}_b[\hat{\rho}_b\hat{\Pi}_{\beta\gamma}]$. For the case of ideal detectors the POVM element $\hat{\Pi}^{\mathrm{ideal}}_{\beta\gamma}$ is a projector $\hat{\Pi}^{\mathrm{ideal}}_{\beta\gamma} = |\chi\rangle\langle\chi|_b$, where $|\chi\rangle_b = \langle\alpha_a|U^\dagger|n_a\rangle|n_b\rangle_b$. For $R = 1/2$ this can be expressed as

$$|\chi\rangle_b = e^{-|\alpha|^2/2}\frac{(\alpha^* - i\hat{b}^\dagger)^{n_a}(\hat{b}^\dagger - i\alpha^*)^{n_b}}{\sqrt{2^{(n_a+n_b)}n_a!n_b!}}|0\rangle_b. \qquad (2)$$

In any realistic scheme one has to account for unavoidable imperfections in the PNR detectors such as loss, nonunit efficiency, and overlap in detector responses. For a given PNR detector, this can be done by considering the detector design [4] or by experimental detector tomography [15]. The time-multiplexed detectors (TMDs) used in our experiments accept states of light contained in pulsed wave packet modes. Each incoming pulse is split into several spatial and temporal modes by a fiber beam splitter network. These modes are subsequently registered by avalanche photodiodes (APDs). Because the TMD alone is not phase sensitive, its operation can be described as a map from the incoming photon-number distribution $\vec{\rho}$ (the diagonal components of the density matrix) to the measured click statistics $\vec{k}$ by $\vec{k} = \mathbf{CL}\vec{\rho}$. Here $\mathbf{L}$ and $\mathbf{C}$ are matrices accounting for loss and the intrinsic detector structure [4], respectively. To calculate the POVM elements implemented by our configurable PNR homodyne detector, the POVMs for TMD detectors D_a and D_b are determined from their $\mathbf{CL}$ matrices (characterized by independent methods). The nth element of the $a(b)$ TMD POVM then replaces the projectors $|n_{a(b)}\rangle\langle n_{a(b)}|$ in Eq. (1) to obtain the final expression for the POVM elements $\hat{\Pi}_{\beta\gamma}$. We note that our TMDs can resolve up to eight photons, setting the number of possible outcomes to 81 and truncating the operator Hilbert space to 9×9 matrices.

By adjusting the local oscillator amplitude and phase, the detector POVM elements $\hat{\Pi}_{\beta\gamma}$ can be tuned to project onto different bases. We illustrate this by calculating $\hat{\Pi}_{\beta\gamma}$ for two particular examples, shown in Fig. 1. For a sufficiently large LO amplitude and detector efficiency (η), the joint click outcomes of the PNR detectors can nearly project onto a single-mode macroscopic quantum superposition state [Fig. 1(b)] or a quadrature-squeezed state [Fig. 1(c)], a feature which suggests our detector can be used both for preparation and direct detection of such quantum states. Figure 1 depicts the Wigner representation of two normalized POVM elements $\hat{\Pi}^{\mathrm{norm}}_{\beta\gamma}$ for $\alpha = 1.5$, $\eta_{a,b} = 90\%$ [16], and 50:50 beam splitter ratio, where (x, p) label the phase-space conjugate variables. Note that a normalized POVM element is a positive definite operator with unit trace, allowing it to have a phase-space representation similar to that of a density matrix. To quantify the state preparation (detection) efficiency for these detector configurations, we calculate the overlap between the target state $\hat{\rho}^{\mathrm{tar}}$ and the normalized POVM projector $\hat{\Pi}^{\mathrm{norm}}_{\beta\gamma}$, by $p = \mathrm{Tr}[\hat{\Pi}^{\mathrm{norm}}_{\beta\gamma}\hat{\rho}^{\mathrm{tar}}]$. In our numerical simulations, $p \approx 80\%$ can increase to values of up to 90% for unit efficiency PNR detectors.

To demonstrate the ability of a PNRHD we experimentally reconstruct various states derived from a coherent-state laser pulse using TMDs for the PNR detectors. The experimental setup, shown in Fig. 2, consists of three main components: the state and local oscillator preparation and the configurable PNRHD. The signal and local oscillator are formed by splitting 90 fs Ti:sapphire laser pulses, centered at 784 nm and cavity dumped to a repetition rate of 250 kHz. In the time-multiplexed detection scheme the APD dead time ($t_D \approx 50$ ns) in conjunction with the total number of temporal modes influences the maximal detection rate. We chose a time delay between temporal modes of 100 ns after which the after-pulsing probability of the APDs drops below 0.1%. This, in combination with electronic time gating, makes after-pulsing effects negligible and reduces dark counts to less than 5 counts/s. The input laser mode is split equally into two optical paths by a half wave plate (HWP) and polarizing beam splitter (PBS), corresponding to V and H polarizations, respectively. The LO path has a HWP and PBS to independently control its amplitude, which is typically set to a small percentage of the total signal. A pair of mirrors in the LO path, placed on

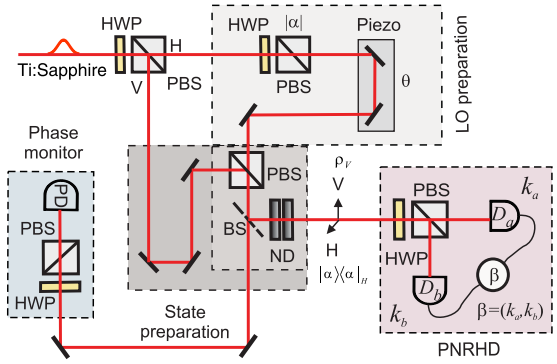

FIG. 2 (color online). Experimental set up for the photon-number-resolving homodyne detector (PNRHD). The output of a Ti:sapphire laser is split into two arms (by a PBS), which eventually correspond to signal $\hat{\rho}$ and LO beams. A piezoelectric moves a mirror to set the phase θ of the LO. Both arms are then recombined and sent through the configurable homodyne detector.

a piezoelectric-controlled translation stage, set the relative phase (θ) between the LO and signal. The two beams are recombined into a single path at a second PBS. A beam sampler (BS) with low reflectivity followed by a set of calibrated neutral density (ND) filters completes the state preparation and directs the signal and LO to a HWP-PBS combination that acts as the homodyne BS in Fig. 1(a). The outputs of the final PBS are sent to TMDs ($D_{a,b}$). The joint detection events are collected using a field-programmable gate array interfaced with a computer. The joint statistics are monitored for 100 different phase settings with a total measurement time of 15 min. The relative phase θ can be monitored using the light transmitted through the BS, which is then interfered using a HWP and PBS and detected at a photodiode. The typical fringe visibility measured at this phase-monitoring step, which indicates the mode match between the signal and LO, was approximately 70%. This relatively low contrast is due to chromatic dispersion in the beam paths and can be improved by placing narrow-band interference filters in the initial laser beam path. Material imperfections and inaccurate calibration in the homodyne HWP-PBS system could in principle be accounted for by the model parameter R; however, such deviations were found to be below 1% in our optical elements and are not considered a significant source of experimental uncertainty in the error analysis.

The local oscillator amplitude $|\alpha| = \langle n_{\mathrm{LO}}\rangle^{1/2}$ is obtained by measuring the average photon number in the LO beam $\langle n^{\mathrm{meas}}\rangle$ and then multiplying by the transmission (T) of a set of calibrated ND filters, so that $(T\langle n^{\mathrm{meas}}\rangle)^{1/2} = \langle n_{\mathrm{LO}}\rangle^{1/2}$, with relative error of approximately 5%, due to the inaccuracy in T. The detector efficiencies ($\eta_{a(b)}$) are obtained by fitting the parameters $\eta_{a(b)}$ in the loss matrix $\mathbf{L}$ which retrieve an average photon number $\langle n_{a(b)}\rangle \approx \langle n_{\mathrm{LO}}\rangle/2$, measured at detector $D_{a(b)}$ when the signal is blocked. For our experiments the fitted detector efficiencies were $\eta_a = 0.10 \pm 0.01$ and $\eta_b = 0.15 \pm 0.02$, where the errors ($\varepsilon_\eta \approx 10\%$) are obtained by propagating the uncertainty in $\langle n_{\mathrm{LO}}\rangle$. The low efficiency, as compared to the APD quantum efficiency ($\approx 60\%$), is due to the single-mode fiber network used to implement the PNR detection. To estimate the effect of these errors in the tomographic reconstructions, we built two POVMs $\{\Pi_{\beta\gamma}^{\max(\min)}\}$ using the maximum (minimum) possible values around the mean for the set of parameters ($\langle n_{\mathrm{LO}}^{\max(\min)}\rangle$, $\eta_a^{\max(\min)}$, $\eta_b^{\max(\min)}$). We found that, while a change of up to 10% in $\langle n_{\mathrm{LO}}\rangle$ does not affect the reconstruction (due to the relatively small amplitude of the LO, as compared to the signal), a change of 10% in the efficiencies propagates into a relative error in the final estimated average photon number $\langle n^{\mathrm{est}}\rangle$ of $\approx 10\%$. In order to estimate the most likely state ($\hat{\rho}^{\mathrm{est}}$) that is compatible with the empirical photocount statistics $p_{\beta\gamma}^{\mathrm{emp}}$, we use a recursive least-squares algorithm to minimize (over $\hat{\rho}^{\mathrm{est}}$) $\sum_{\beta\gamma}(p_{\beta\gamma}^{\mathrm{emp}} - \mathrm{Tr}[\hat{\Pi}_{\beta\gamma}\hat{\rho}^{\mathrm{est}}])^2$, subject to the constraints $\hat{\rho}^{\mathrm{est}} \geq 0$ and $\mathrm{Tr}[\hat{\rho}^{\mathrm{est}}] = 1$ [7].

The first class of states to be examined were the phase-averaged coherent states. Here 20 evenly distributed LO phases θ are chosen between 0 and 2π for the data acquisition. Figures 3(a)–3(c) show the experimentally reconstructed Wigner functions and corresponding contour plots for three different phase-averaged coherent states. The Wigner functions are rotationally symmetric and centered about the origin, as expected for such states. To quantify the error in the estimated state we calculate the variance Δ between the two extreme estimated states $\hat{\rho}^{\max(\min)}$, obtained using the two extreme POVMs $\{\Pi_{\beta\gamma}^{\max(\min)}\}$, by $\Delta = 1 - F$, with $F = |\mathrm{Tr}(\sqrt{(\sqrt{(\hat{\rho}^{\min})}\hat{\rho}^{\max}\sqrt{(\hat{\rho}^{\min})}))}|^2$ the fidelity between the two extreme estimated density matrices. Figure 3(d) shows an extreme POVM element for outcome $\beta = (1, 0)$ and Fig. 3(e) shows the difference between $\hat{\Pi}_{\beta\gamma}^{\max} - \hat{\Pi}_{\beta\gamma}^{\min}$. Such POVM elements do not look exactly like a projector onto a

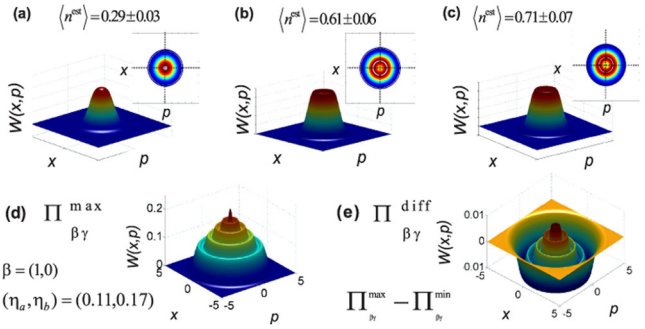

FIG. 3 (color online). Wigner function and corresponding contour plot (inset) of the experimentally reconstructed phase-averaged weak coherent states, with average photon numbers $\langle n^{\mathrm{est}}\rangle$ equal to (a) 0.29 ± 0.03, (b) 0.61 ± 0.06, and (c) 0.71 ± 0.07. (d) One extreme POVM element used in the error estimation $\hat{\Pi}_{\beta\gamma}^{\max}$, (e) difference between two extreme POVM elements $\hat{\Pi}_{\beta\gamma}^{\mathrm{diff}} = \hat{\Pi}_{\beta\gamma}^{\max} - \hat{\Pi}_{\beta\gamma}^{\min}$.

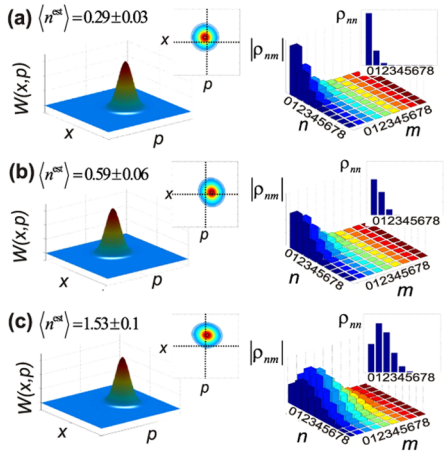

FIG. 4 (color online). Wigner function (left) and amplitude of the density matrix in the photon-number basis $|\hat{\rho}_{nm}|$ (right) for experimentally reconstructed weak coherent states. Here (x, p) labels the quadratures and (n, m) labels the photon numbers. Insets show corresponding contour plot (left) and diagonal matrix elements (right). Rows correspond to an average photon number $\langle n^{\text{est}} \rangle$ of (a) 0.29 ± 0.03, (b) 0.59 ± 0.06, and (c) 1.53 ± 0.1.

single photon state. This is due to the low detector efficiency which mixes POVM elements corresponding to higher photon numbers. Additionally, as a second figure of merit, we quantify the proximity of the reconstructed state $\hat{\rho}^{\text{est}}$ with an ideal phase-averaged coherent state $\hat{\rho}^{\text{PA}}$ of average photon number $\langle n^{\text{est}} \rangle$, using the fidelity F, by replacing $\hat{\rho}^{\text{max(min)}}$ by $\hat{\rho}^{\text{PA(est)}}$. The variances and fidelities (Δ, F) resulted in (a) $(0.004, 0.985)$, (b) $(0.010, 0.973)$, and (c) $(0.027, 0.954)$, respectively. Note that the error increases with the average photon number, an expected effect which is due to the truncation of the Fock-state space present in the modeled POVMs.

Next, in order to test the phase sensitivity of this detector, several coherent states were tomographically reconstructed. Figure 4 shows the experimentally reconstructed Wigner function $W(x, p)$ and density-matrix amplitude $|\hat{\rho}|$, for coherent states of different average photon numbers. The variance and fidelity are used again as figures of merit of the state reconstruction, with $\hat{\rho}^{\text{CS}}$ the density matrix for an ideal coherent state with average photon number $\langle n^{\text{est}} \rangle$ and phase θ^{est} taking the place of $\hat{\rho}^{\text{PA}}$, $\langle n^{\text{est}} \rangle$ was obtained from the diagonal elements of $\hat{\rho}^{\text{est}}$, and θ^{est} was obtained as an average over the off-diagonal matrix elements using $\rho^{\text{est}}_{n,m} = \langle n^{\text{est}} \rangle^{(n+m)/2} e^{-(\langle n^{\text{est}} \rangle)} e^{-i(n-m)\theta^{\text{est}}} / \sqrt{n!m!}$. We found (Δ, F) equal to (a) $(0.002, 0.999)$, (b) $(0.010, 0.998)$, and (c) $(0.010, 0.997)$, respectively.

In conclusion, we have introduced a highly adaptable homodyne detection scheme with PNR detectors. This approach bridges the gap between phase-sensitive weak-field homodyne techniques and PNR detection, opening a new avenue of research and realm of applicability for PNR technology. The various states the detector can directly project onto (squeezed states, macroscopic quantum superposition states, and displaced-Fock states) make it useful not only for state detection, but also for state preparation, a direction which is currently being explored by our group. The detector has proven to be effective for state tomography as demonstrated by the experimental reconstruction of weak coherent and phase-averaged weak coherent states.

This work was supported by the EPSRC through the QIP IRC, by the EC under QAP, by the IST directorate, and by the Royal Society. H. C. R. is supported by the European Commission under the Marie Curie Program and by the Heinz-Durr Stipendienprogamm of the Studienstiftung des deutschen Volkes.

*g.puentes1@physics.ox.ac.uk

[1] Bureau International des Poids et Mesures, The International System of Units (SI), 2008, 8th ed., http://www.bipm.org/en/si/si_brochure.
[2] J. L. O'Brien *et al.*, Phys. Rev. Lett. **93**, 080502 (2004).
[3] D. T. Smithey, M. Beck, M. G. Raymer, and A. Faridani, Phys. Rev. Lett. **70**, 1244 (1993).
[4] D. Achilles *et al.*, J. Mod. Opt. **51**, 1499 (2004).
[5] A. S. Holevo, *Probabilistic and Statistical Aspects of Quantum Theory* (North-Holland, Amsterdam, 1982).
[6] W. P. Schleich, *Quantum Optics in Phase Space* (Wiley, Berlin, 2001).
[7] R. L. Kosut, I. A. Walmsley, and H. Rabitz, arXiv:quant-ph/0411093.
[8] S. A. Babichev, B. Brezger, and A. I. Lvovsky, Phys. Rev. Lett. **92**, 047903 (2004).
[9] G. Zambra and M. G. A. Paris, Phys. Rev. A **74**, 063830 (2006); M. Takeoka, M. Sasaki, and N. Lütkenhaus, Phys. Rev. Lett. **97**, 040502 (2006); K. Banaszek, A. Dragan, K. Wódkiewicz, and C. Radzewicz, Phys. Rev. A **66**, 043803 (2002); L. S. Phillips, S. M. Barnett, and D. T. Pegg, Phys. Rev. A **58**, 3259 (1998); D. Mogilevtsev, Z. Hradil, and J. Peřina, Quantum Semiclass. Opt. **10**, 345 (1998); S. Wallentowitz and W. Vogel, Phys. Rev. A **53**, 4528 (1996); K. Banaszek and K. Wódkiewicz, Phys. Rev. Lett. **76**, 4344 (1996).
[10] G. Zambra *et al.*, Phys. Rev. Lett. **95**, 063602 (2005); K. Banaszek, C. Radzewicz, K. Wódkiewicz, and J. S. Krasiński, Phys. Rev. A **60**, 674 (1999).
[11] A. Divochiy *et al.*, Nat. Photon. **2**, 302 (2008); B. E. Kardyna *et al.*, Nat. Photon. **2**, 425 (2008).
[12] S. Huver, C. Wildfeuer, and J. Dowling, Phys. Rev. A **78**, 063828 (2008).
[13] M. Horodecki, P. Horodecki, and R. Horodecki, Phys. Lett. A **223**, 1 (1996).
[14] K. L. Pregnell and D. T. Pegg, Phys. Rev. A **66**, 013810 (2002).
[15] J. S. Lundeen *et al.*, Nature Phys. **5**, 27 (2009).
[16] An efficiency of 90% is achievable with current PNR detectors [A. E. Lita, A. J. Miller, and S. W. Nam, Opt. Express **16**, 3032 (2008)].